Dalton Transactions

ROYAL SOCIETY OF CHEMISTRY

PAPER

View Article Online
View Journal | View Issue



Cite this: *Dalton Trans.*, 2026, **55**, 1360

# A nickel incorporated triazine-based porous organic polymer for the electrocatalytic methanol oxidation reaction

Indrani Pramanick,[a] Samarpita Das,[a] Bhabani Malakar,[b] Sanjana Banerjee,[a] Asim Bhaumik *[b] and Papu Biswas *[a]

The methanol oxidation reaction (MOR) has been recognized as a promising anode reaction for hydrogen production through electrochemical water splitting. Moreover, the methanol oxidation reaction (MOR) is a key electrode reaction in direct methanol fuel cells (DMFCs). Thus, the development of non-noble metal-based, cost-effective, and efficient electrocatalysts for the methanol oxidation reaction (MOR) is crucial. Herein, a facile polycondensation strategy to fabricate a cost-efficient, triazine-based porous organic polymer (MDF) has been developed by a reaction between 2,6-diformyl-4-methylphenol and melamine. Nickel(II) was incorporated into the polymer by reacting MDF with nickel(II) acetate in dimethyl formamide (DMF). The nickel incorporated catalyst (Ni-MDF) exhibited superior electrocatalytic MOR activity. The MDF and Ni-MDF materials possess high specific surface areas of 500.8 $m^2 g^{-1}$ and 321.86 $m^2 g^{-1}$, respectively, and exceptional thermal stability. The MOR activity reveals the excellent catalytic performance of the Ni-MDF catalyst with a low onset potential of 1.36 V (*vs.* RHE) and an overpotential of 160 mV (*vs.* RHE) to achieve 10 mA $cm^{-2}$ current density. The as-synthesized Ni-MDF catalyst exhibited a Tafel slope of 24.4 mV $dec^{-1}$ and a current density of 112 mA $cm^{-2}$ at 1.68 V *vs.* RHE. The catalyst demonstrates excellent chronoamperometric and chronopotentiometric stability. The faradaic efficiency (FE) of the Ni-MDF-2 catalyst for the production of value added formate at the anode has been evaluated. Moreover, the potential required for the Pt/C||Ni-MDF-2 electrolyzer for hydrogen generation has also been investigated.

Received 26th September 2025,
Accepted 10th December 2025

DOI: 10.1039/d5dt02306h

rsc.li/dalton



## Introduction

The ever-growing concern regarding environmental pollution and global warming due to the extensive use of fossil fuels has compelled scientists to explore environment-friendly energy resources. The green hydrogen generated through electrochemical water splitting using renewable energy sources is considered a prospective eco-friendly alternative energy source.[1] The exceptional environmental friendliness and high energy density make hydrogen ideal for sustainable development. Consequently, water electrolysis has drawn significant attention from researchers over the years.[2–5] The electrochemical splitting of water comprises two half-cell reactions: the HER (hydrogen evolution reaction) at the cathode and the OER (oxygen evolution reaction) at the anode.[6–11] However, the crucial OER process often encounters a sluggish proton-coupled electron transport process along with high overpotential, making the efficiency of the entire water-splitting process inefficient. An energy-efficient approach for improving hydrogen production efficacy is substituting the OER with an alternative anodic reaction with reduced oxidation potential. Subsequently, efforts have been made to substitute the OER with the oxidation of small molecules, such as alcohols, hydrazine, urea, *etc.*[12–20] Among small molecules, methanol oxidation has garnered significant attention owing to its affordability, high energy density, cost-effectiveness, and low carbon emission. Moreover, the methanol oxidation reaction (MOR) is a fundamental electrode reaction in direct methanol fuel cells (DMFCs). DMFCs have gained tremendous attention as potential energy conversion devices due to their superior energy conversion properties, easy transportability, and mild operating temperatures.[21–23] The electrocatalysts based on Pt, Pd, Rh, Ru, Ir, and Au demonstrate remarkable MOR activity.[24–29]

Despite the outstanding activity of noble-metal-based catalysts, their widespread practical use has been significantly impeded by their high cost, scarcity, and lack of durability. Furthermore, noble metal-based electrocatalysts are susceptible to poisoning by intermediate CO, resulting in a significant deterioration in catalytic activity.[30–36] Accordingly, considerable efforts have been made to develop non-noble metal-

[a]*Department of Chemistry, Indian Institute of Engineering Science and Technology, Shibpur, Howrah 711 103, West Bengal, India.*
*E-mail: papubiswas_besus@yahoo.com, papu.chem@faculty.iiests.ac.in*
[b]*School of Material Sciences, Indian Association for the Cultivation of Science, Kolkata 700 032, West Bengal, India*

based, cost-effective, and efficient electrocatalysts with excellent performance for the methanol oxidation reaction (MOR).

In recent years, Ni-based electrocatalysts have emerged as potential alternatives for the MOR due to their low cost, abundance, high catalytic activity, and stronger resistance to CO poisoning.[32–34,36,37] Consequently, many nickel-based electrocatalysts have been developed and explored, such as Nis/NiO,[38] $Ni_2P$,[39] Ni/NiO,[40] nickel boride/nickel,[41] NiM-layered double hydroxide (M = Mn and Fe),[42] Os-doped $Ni_xP$ on N-doped carbon,[43] bimetallic NiCo MOF,[44] Ni-MOF on $Ni(OH)_2$,[45] Ni(II)-incorporated porphyrin-based covalent organic polymer,[46] NiO grown on nickel foam (NF),[47] $Ni_3S_2$@CuAg,[48] $Ni(OH)_2$-$Co_3O_4$,[49] $Ce_{1-x-y}Zr_xNi_yO_{2-\delta}$ catalyst,[33] $NiZn_x$@CuO nanoarray,[32] $NiCo_2O_4/Ti_3C_2T_x$-MXene,[30] MXene-based Pd/Ni/Cu nanocatalyst,[50] CNTs@CoO–$Ni(OH)_2$,[36] and NiCu-LDH/MXene nanocomposites.[51]

Recently, covalent triazine frameworks (CTFs) along with triazine-based covalent organic frameworks (COFs) and porous organic polymers (POPs) have gained considerable popularity as electrocatalysts for energy conversion and storage, $CO_2$ reduction *etc*.[52] Bhaumik and his group reported triazine-based COFs for the HER[53] and capacitive energy storage.[54] Bhunia *et al.* reported CTFs for photocatalytic $H_2$ production[55] and $CO_2$ reduction.[56] The research groups of Zhang, He, and Du collaboratively investigated the bifunctional electrocatalyst activity of a triazine-based POP for zinc–air batteries.[57] Kundu and his coworkers explored the metalation-induced bifunctional OER and HER activity of a triazine-based COF.[58] Dey and his group revealed the ORR activity of a triazine-based COF.[59]

Despite substantial progress having been made in replacing noble metal-based catalysts for the MOR with nickel-based composites, the use of nickel-incorporated COFs/POPs as catalysts for the MOR in alkaline media remains mostly unexplored. Moreover, replacing the OER with the MOR at the anode during hydrogen production at the cathode is not only an energy-saving process but also produces value-added formate at the anode. Accordingly, we aim to explore the efficacy of nickel-incorporated Ni-MDF, where nickel is incorporated in an N-rich amine-linked triazine-based porous organic polymer (MDF), for the MOR reaction and formate production. The MDF was prepared through polycondensation of melamine and 2,6-diformyl-4-methylphenol. The $Ni^{2+}$-incorporated electrocatalyst, Ni-MDF-2, with 4.72 atom% of Ni exhibited the highest MOR activity. Notably, the Ni-MDF-2 catalyst exhibited excellent catalytic activity with a low onset potential of 1.36 V and a low overpotential of 160 mV to achieve a current density of 10 mA $cm^{-2}$. The Ni(II)-incorporated catalyst (Ni-MDF) demonstrates efficacy for the electrocatalytic MOR in an alkaline medium with good faradaic efficiency for formate production. The efficiency of the Pt/C|| Ni-MDF-2 electrolyzer was also evaluated. Moreover, operando electrochemical impedance spectroscopy (EIS) with post-catalytic XPS and Raman spectroscopy were utilized to verify the formation of $Ni^{3+}$ species and the reaction kinetics of the MOR.

# Experimental section

### Materials and methods

All the reagents were of analytical grade and used without any purification. Melamine (99%), Nafion (97%), potassium hydroxide (99%), and nickel(II) acetate tetrahydrate (99%) were purchased from Sigma-Aldrich Chemicals Private Limited (Merck). Dimethylformamide (anhydrous), dimethyl sulphoxide, and methanol were purchased from Spectrochem Pvt Ltd. 2,6-Diformyl-4-methylphenol (DMP) was synthesized using a previously reported method.[60] The methods and fabrication related to the electrochemical study and material characterization are described in the SI.

### Synthesis of an N-rich aminal-linked triazine-based porous organic polymer (MDF)

A mixture of 2,6-diformyl-4-methylphenol (6 mmol, 0.984 g) and melamine (4 mmol, 0.504 g) dissolved in 40 mL of dry DMSO was taken in a 100 mL round-bottom flask. The resulting mixture was heated to 160° C under vigorous stirring in a nitrogen atmosphere for 72 h. After completion of the reaction, the resulting solution was allowed to cool down to room temperature. The solid product was filtered and washed with dimethylformamide (DMF), acetone, methanol, and dichloromethane. The product was then dried at 50° C under vacuum overnight. The crude product was purified by Soxhlet extraction using tetrahydrofuran and acetone to obtain an off-white product. The yield of the reaction was found to be 1.026 g.

### Synthesis of Ni-MDF-0.5

Nickel(II) acetate tetrahydrate (0.5 mmol, 0.124 g) was dissolved in 30 mL of dimethyl formamide solution in a round-bottom flask, and 0.2 g of MDF was added to it. The resulting mixture was refluxed for 6 h under continuous stirring. After completion of the reaction, the reaction mixture was cooled to room temperature and the residue was isolated by filtration. The collected product was washed successively with DMF and methanol and dried under vacuum overnight at 60° C to obtain Ni-MDF. Three more samples were prepared with 1, 2, and 4 mmol of nickel(II) acetate following the above method. The samples were named as Ni-MDF-*X* (*X* = 0.5, 1, 2, and 4).

# Results and discussion

The microporous polyaminal network MDF was synthesized through a "one-step" catalyst-free polycondensation reaction between 2,6-diformyl-4-methylphenol (DMP) and melamine. Scheme 1 shows the synthesis of MDF and Ni-MDF. The incorporation of nickel(II) was accomplished by a reaction between nickel(II) acetate and MDF in DMF.

The formation of aminal linkages in the polymer networks was confirmed by FT-IR and solid-state $^{13}C$ MAS NMR spectroscopy. The FT-IR spectra (Fig. 1a) reveal the C=O stretching band at 1670 $cm^{-1}$ attributed to the carbonyl signal of DMP, disappearing after polymerization. The $NH_2$ stretching band

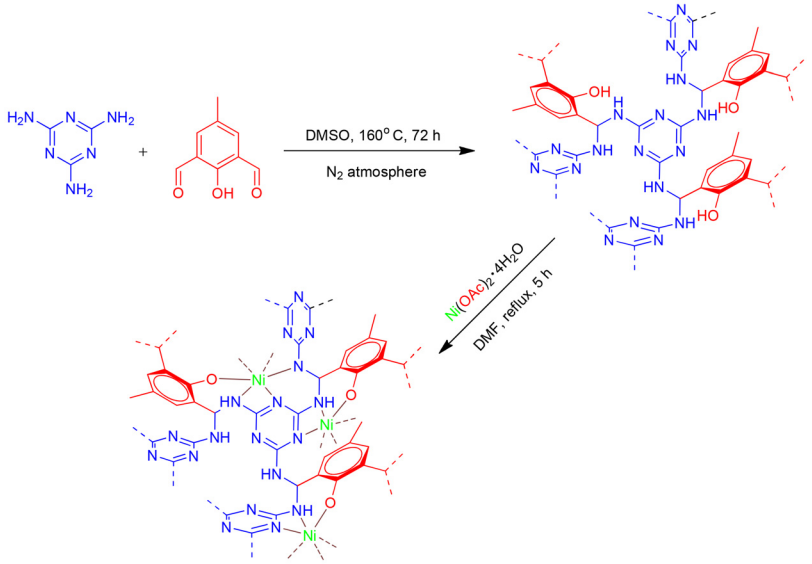


**Scheme 1** Synthesis of the N-rich aminal-linked triazine-based porous organic polymer (MDF) and Ni-MDF.

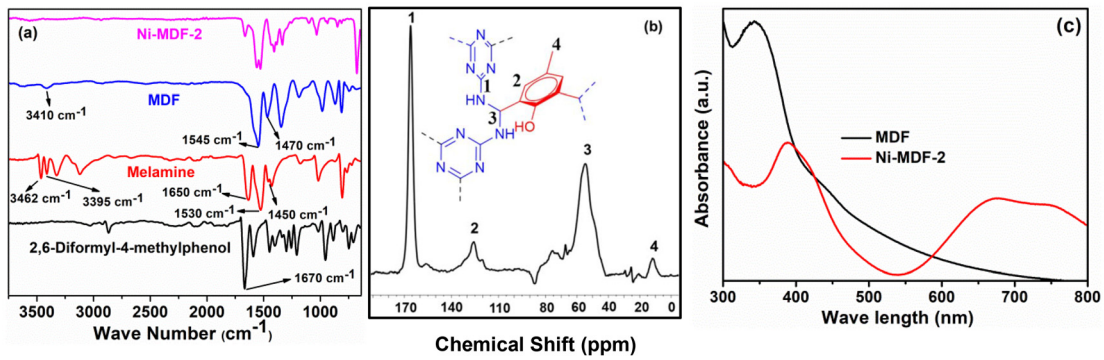


**Fig. 1** (a) FT-IR spectra of 2,6-diformyl-4-methylphenol, melamine, MDF, and Ni-MDF-2, (b) $^{13}$C CP-MAS spectra of MDF, and (c) DRS spectra of MDF and Ni-MDF-2.

(3462 $cm^{-1}$ and 3395 $cm^{-1}$) and $NH_2$ deformation band (1650 $cm^{-1}$) of the residual primary amine group are absent in the polymer. The characteristic bands of the triazine ring assigned to quadrant (1530 $cm^{-1}$) and semicircle (1450 $cm^{-1}$) stretching appear in the spectra of both melamine and the polymer, which indicates that melamine is successfully incorporated in the MDF. However, in the polymer the quadrant and semicircle stretching frequencies are observed at 1545 and 1470 $cm^{-1}$, respectively. Moreover, the emergence of a broad band around 3410 $cm^{-1}$ indicates the polymer linkage through the C–N–H bond between melamine and dialdehyde.[61] The quadrant and semicircle stretching frequencies split into two different peaks after the inclusion of nickel(II) in the polymer.

The solid-state $^{13}$C CP-MAS NMR spectrum (Fig. 1b) also confirms the formation of the polymer, as shown in Fig. 1b. The peaks observed at 166 and 125.8 ppm confirm the presence of the triazine and benzene rings, respectively. The $^{13}$C signal at around 55 ppm appeared for the carbon atom at the secondary amine linkages formed after the condensation. The peak at 11.9 was observed due to the methyl group. The incorporation of nickel(II) in the polymer was further established from the diffuse reflectance spectroscopy (DRS) of MDF and Ni-MDF (Fig. 1c). Ni-MDF-2 exhibited two peaks in DRS, an intense peak at about 390 nm and another peak around 675 nm with a shoulder. The paramagnetic nature of Ni-MDF-2 due to incorporation of Ni(II) was established by the room-temperature magnetic moment value of 2.96 BM. The room-temperature magnetic moment value and d–d band energy indicate an octahedral geometry around Ni(II). The d–d bands may be assigned for $^3A_{2g} \rightarrow {}^3T_{1g}(P)$ and $^3A_{2g} \rightarrow {}^3T_{1g}(F)$, $^1E_g$ transitions at 400 and 675 nm, respectively, assuming an octahedral geometry around nickel(II) in the MDF polymer.

The morphology and nano-structural features of the catalysts were analyzed using FESEM and TEM techniques. The FESEM images demonstrate the agglomerated quasi-spherical morphology of MDF (Fig. S1) and Ni-MDF-2 (Fig. 2a). The TEM

 

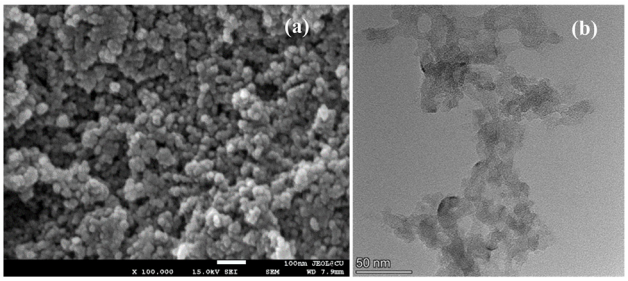


Fig. 2 (a) FE-SEM and (b) TEM images of Ni-MDF-2.

image also confirms the irregular nano-spherical structure of Ni-MDF-2 (Fig. 2b). The SEM-EDX mapping confirms the homogeneous distribution of Ni, N, and O within the MDF framework (Fig. S2). Furthermore, the elemental mapping obtained using a high-angle annular dark field scanning transmission electron microscope (HAADF-STEM) shows the uniform distribution of Ni, N, and O within the MDF (Fig. S3).

XPS analysis was utilized to determine the chemical composition and electronic structure of the elements present in Ni-MDF-2. The XPS survey spectrum, displayed in Fig. S4, confirms the coexistence of Ni, C, N, and O. The XPS peaks were calibrated to the C1s peak at 284.6 eV. The high-resolution XPS spectrum of Ni 2p shows four significant peaks (Fig. 3a). Two peaks at 856.1 eV and 873.6 eV are attributed to Ni $2p_{3/2}$ and Ni $2p_{1/2}$ of the $Ni^{2+}$ state. The additional two peaks at 861.4 and 879.4 eV are the respective satellite peaks of the $Ni^{2+}$ state. The deconvoluted spectrum of C1s exhibits two prominent peaks at 284.6 eV and 288.4 eV (Fig. 3b), which are ascribed to C–C and C–O bonds, respectively. A small hump at 286.2 eV appears due to C–N functionalities (Fig. 3b). The O 1s high-resolution spectrum exhibits a major peak at 531.6 eV due to the presence of phenolic OH and trapped water molecules in MDF, as depicted in Fig. 3c.[62] A low-intensity peak at a higher binding energy of 532.7 eV could be attributed to the oxygen atom bonded to Ni(II).[63] The high-resolution deconvoluted N 1S spectrum shown in Fig. 3d consists of four peaks at binding energies of 398.4, 399.6, 399.9, and 400.9 eV. The peak at 398.4 eV corresponds to the –N= bond of the triazine moiety, and the peak at 399.9 eV is attributed to the –NH– bond of imine.[62] Two low-intensity peaks at 399.6 and 400.9 eV were observed due to nickel-bonded triazine and imine nitrogen, respectively.[64] The nickel loading was found to be 4.72 atom% from the XPS measurements.

The porosity and specific surface areas of the MDF and Ni-MDF-2 catalysts were evaluated using $N_2$ adsorption/desorption isotherms at 77 K. The $N_2$ sorption isotherms of the as-synthesized polymers exhibited a sharp increase in gas uptake at very low relative pressure ($P/P_0$), suggesting typical characteristics of a microporous material (Fig. 4a). The MDF and Ni-MDF-2 materials exhibited BET (Brunauer–Emmett–Teller) surface areas of 500.8 $m^2\ g^{-1}$ and 321.864 $m^2\ g^{-1}$, respectively. The inclusion of nickel(II) sites resulted in a decrease in surface area. The pore size distributions of MDF and Ni-MDF-2 were assessed using nonlocal density functional theory (NLDFT). As illustrated in Fig. 4b, both MDF and Ni-MDF-2 materials displayed characteristic micro porosity, having predominant pore dimensions of 1.40 nm and 0.98 nm, respectively.

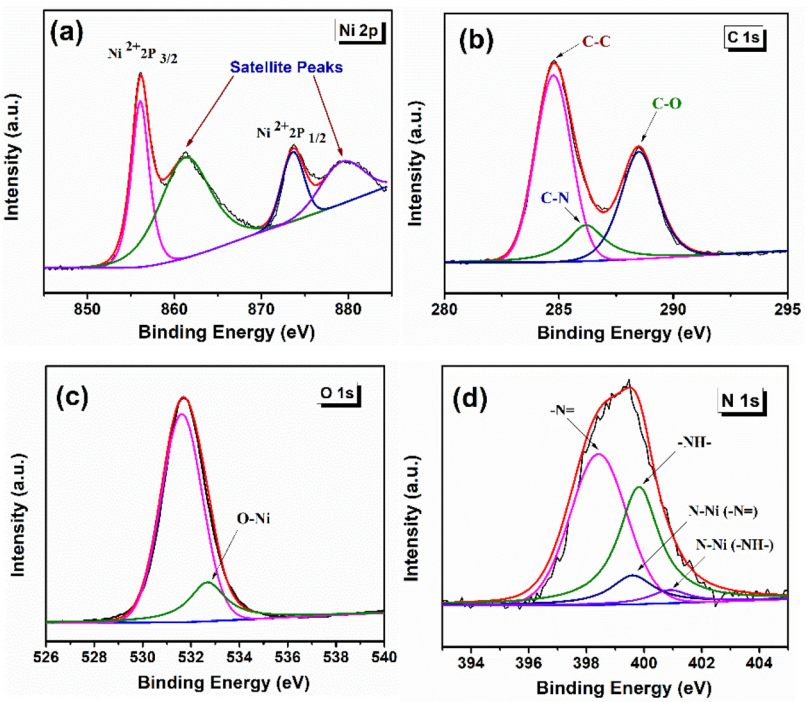


Fig. 3 High-resolution XPS spectra for (a) Ni 2p, (b) C 1s, (c) O 1s, and (d) N 1s of Ni-MDF-2.

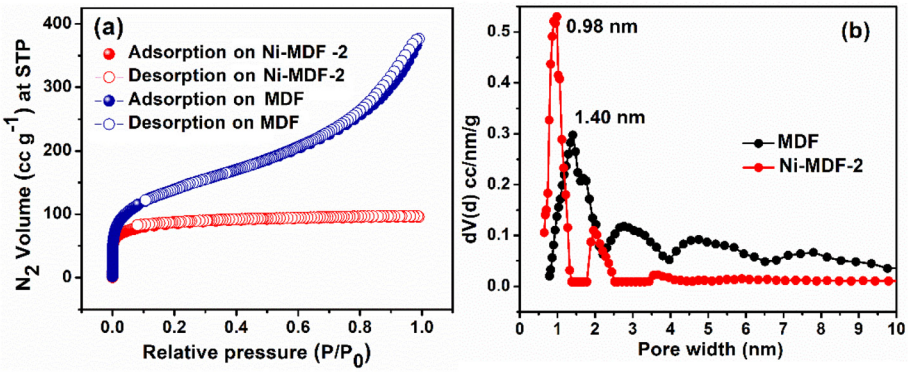


Fig. 4 (a) $N_2$ adsorption–desorption isotherms of MDF and Ni-MDF-2 at 77 K and (b) pore size distribution by the NLDFT method.

Thermogravimetric analysis (TGA) was conducted to assess the thermal stability of MDF and Ni-MDF-2 catalysts. As depicted in Fig. 5, the MDF polymer is stable up to 365 °C with only ~25% weight loss. The polymer starts to lose weight sharply after 365 °C. However, the TGA curve of Ni-MDF-2 exhibits three distinct mass losses up to 700 °C. Ni-MDF-2 shows thermal stability up to 260 °C with merely 12% mass loss, above which a steady and sharp weight loss is observed up to 500 °C. Ni-MDF-2 retains ~26.5% of its original mass up to 700 °C.

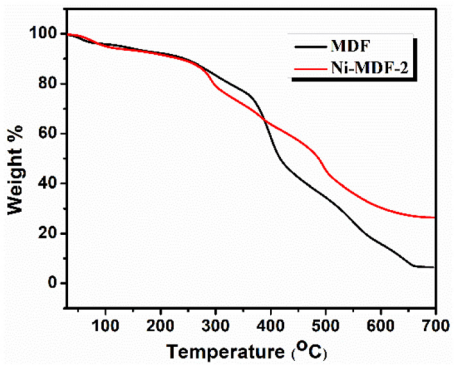


Fig. 5 TGA analysis of MDF and Ni-MDF-2.

The powder XRD patterns of MDF and Ni-MDF-2 (Fig. 6) exhibited two very broad peaks centered at $2\theta$ = 21° and 40°, which indicate the amorphous nature of the materials. The weight percentages of Ni loading in the catalysts were estimated using XRF and are shown in Table S1.

### Methanol electrooxidation activity of the catalyst

The methanol electrooxidation activities of the as-prepared catalysts were then evaluated by cyclic voltammetric (CV) measurements in 1.0 M KOH and 0.5 M methanol. As shown in Fig. 7a, in the absence of methanol, the CV of the Ni-MDF-2 catalyst displayed distinct redox peaks in both cathodic and anodic scans. The peak at 1.39 V (*vs.* RHE) during the anodic scan is attributed to the oxidation of $Ni^{2+}$ to $Ni^{3+}$, and the peak at 1.28 V (*vs.* RHE) during the cathodic scan is indicative of the reduction of $Ni^{3+}$ to $Ni^{2+}$. Moreover, the CV of Ni-MDF-2 in the presence of methanol exhibited a significant rise in anodic current density, confirming the activity of the catalyst towards the MOR. The Ni-MDF-2 catalyst required a very low overpotential of 160 mV to achieve 10 mA $cm^{-2}$ with a low onset potential of 1.36 V (*vs.* RHE). Notably, Ni-MDF-2 requires an overpotential of 410 mV to achieve 10 mA $cm^{-2}$ current density in a 1.0 M KOH solution. However, the addition of 0.5 M methanol results in a much lower overpotential of 160 mV to achieve the same current density. Thus, the addition of methanol reduces the required overpotential by approximately 250 mV. The

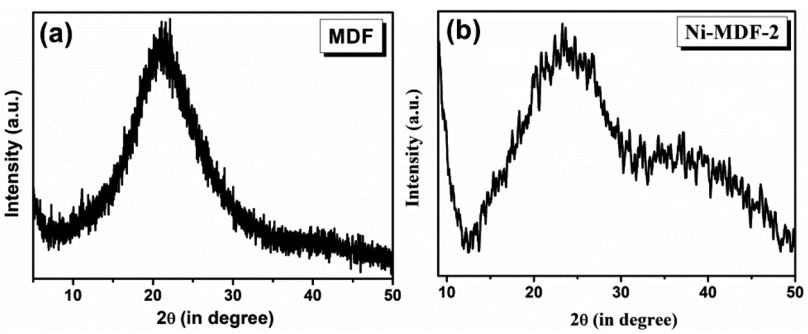


Fig. 6 Powder XRD patterns of (a) MDF and (b) Ni-MDF-2.

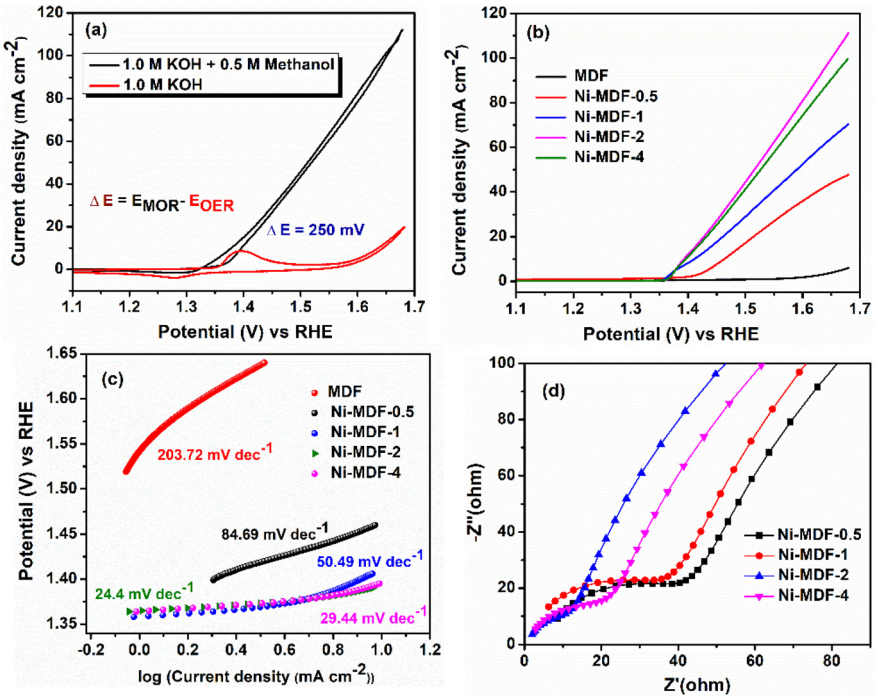


**Fig. 7** (a) CV curves of Ni-MDF-2 in the presence and absence of 0.5 M methanol in 1.0 M KOH electrolyte at a scan rate of 50 mV $s^{-1}$. (b) LSV curves of MDF, Ni-MDF-0.5, Ni-MDF-1, Ni-MDF-2, and Ni-MDF-4, in 0.5 M methanol containing 1.0 M KOH at 50 mV $s^{-1}$ scan rate. (c) Tafel plots of MDF, Ni-MDF-0.5, Ni-MDF-1, Ni-MDF-2, and Ni-MDF-4 at a 5 mV $s^{-1}$ scan rate. (d) Nyquist plot of Ni-MDF-0.5, Ni-MDF-1, Ni-MDF-2, and Ni-MDF-4 at 1.39 V *vs.* RHE in 1.0 M KOH and 0.5 M methanol.

activities of the MDF and all the catalysts toward MOR were also evaluated by linear sweep voltammetry (LSV) and compared to that of Ni-MDF-2 (Fig. 7b). In the presence of 0.5 M methanol, MDF, Ni-MDF-0.5, Ni-MDF-1, and Ni-MDF-4 catalysts exhibited higher overpotential and lower current density than Ni-MDF-2. Fig. S5 shows the CV curves of MDF and the Ni-MDF catalysts in the presence of 1.0 M KOH and 0.5 M methanol. The Tafel slopes were evaluated to acquire detailed insight into the kinetics of the MOR. Tafel slopes for all the catalysts were obtained from LSV in the presence of 1.0 M KOH and 0.5 M methanol at a scan rate of 5 mV $s^{-1}$ (Fig. 7c). The Ni-MDF-2 catalyst displays a Tafel slope of 24.4 mV $dec^{-1}$, which is significantly smaller compared to those of MDF (203.72 mV $dec^{-1}$), Ni-MDF-0.5 (84.69 mV $dec^{-1}$), Ni-MDF-1 (50.49 mV $dec^{-1}$), and Ni-MDF-4 (29.44 mV $dec^{-1}$). The lower Tafel slope indicates the faster electron transport and better electrocatalytic activity of the Ni-MDF-2 catalyst for the MOR. To assess the electrical conductivity and ion transport kinetics, an electrochemical impedance spectroscopy (EIS) study was performed in a solution containing 1.0 M KOH and 0.5 M methanol at 1.39 V (Fig. 7d). The obtained data were fitted using equivalent circuits, as shown in the inset of Fig. S6a and b. The different fitted parameters for Ni-MDF-2 and MDF are summarized in Tables S2 and S3. The Ni-MDF-2 catalyst exhibits a lower charge transfer resistance ($R_{CT}$) of 9.27 Ω compared to the other Ni-MDF catalysts (Table S4). Table S5 shows the comparison of the electrocatalytic activity of MDF and the Ni-MDF catalysts toward the MOR.

To compare the catalytic activity of the Ni-MDF catalyst with that of the benchmark Pt catalyst, cyclic voltammetric (CV) measurements were performed in 1.0 M KOH and 1.0 M methanol, employing a 5% Pt on graphitic carbon (Pt/C) catalyst. Although the Pt/C catalyst exhibited lower onset potential and overpotential, it showed inferior current density under the same conditions (Fig. S7). Moreover, Pt-based catalysts often suffer from the CO poisoning problem. Furthermore, the efficacy of the Ni-MDF-2 catalyst for electrochemical methanol oxidation was assessed in the presence of 0.5 M $H_2SO_4$ and 0.5 M methanol (Fig. S8). The catalyst showed much inferior activity in the acidic medium, probably due to catalyst degradation in the presence of acid.

The effect of the analyte concentration on catalytic activity was explored by cyclic voltammetric measurements of the Ni-MDF-2 catalyst in 1.0 M KOH solution with different methanol concentrations (Fig. S9a). Fig. S9b shows the variation of overpotential required to achieve 10 mA $cm^{-2}$ current density against the methanol concentration. Fig. S9b shows that the overpotential decreases significantly up to 0.5 M methanol concentration, but after that, the overpotential increases. Furthermore, the anodic current increases rapidly up to 0.5 M methanol. However, above 0.5 M methanol, the anodic current decreases slightly (Fig. S9a), implying saturation of the MOR kinetics. The dependence of the catalytic efficiency of the Ni-MDF-2 catalyst on the concentration of KOH was also evaluated by performing CV in 0.5 M methanol solution with different concentrations of KOH (Fig. S9c). Fig. S9c shows that

the overpotential decreases and the anodic current density increases with increasing KOH concentration up to 1.0 M. However, no further improvement was observed with the increase in KOH concentration. Thus, 0.5 M methanol in 1.0 M KOH was chosen as the optimized conditions for the methanol oxidation reaction.

To evaluate the effect of scan rates on the OER and MOR process, CV of Ni-MDF-2 was performed at different scan rates ranging from 10 mV $s^{-1}$ to 100 mV $s^{-1}$ (Fig. S10). Fig. S10a shows the CV curves at various scan rates in 1.0 M KOH electrolyte. As depicted in Fig. S10b, the anodic current density at 1.40 V increases linearly with an increase in the square root of the scan rate for the OER, indicating that the OER is a diffusion-controlled process. The CV curves of the Ni-MDF-2 catalyst in the presence of 1.0 M KOH and 0.5 M methanol at various scan rates are shown in Fig. S10c. Fig. S10d illustrates the relationship between the anodic peak current density at 1.66 V and the square root of the scan rate. The linear nature of the curve suggests that the MOR process is also diffusion-controlled.

The electrochemically active surface area (ESCA) is a significant parameter for gaining insight into catalytic activity. The ECSAs of the catalysts were evaluated from the electrochemical double-layer charge capacitance ($C_{dl}$) associated with the catalytic surface. The double-layer capacitance ($C_{dl}$) was obtained by measuring the non-faradaic current associated with double-layer charging from scan-rate-dependent cyclic voltammograms. The double-layer charging current ($i_c$) can be expressed as the product of the scan rate ($v$) and the electrochemical double-layer capacitance ($C_{dl}$), according to the equation $i_c = vC_{dl}$. Consequently, a plot of $i_c$ *versus* $v$ yields a linear relationship, with the slope corresponding to $C_{dl}$. The ECSA was then calculated using the relation ECSA = ($C_{dl}/C_s$), where $C_s$ denotes the specific capacitance of the material per unit area under identical electrolyte conditions. The specific capacitance ($C_s$) is assumed to be 0.040 mF $cm^{-2}$ in 1.0 M NaOH.[65,66] The ECSA values were found to be 0.4725, 2.336, 3.325, 7.665, and 6.606 $cm^2$ for MDF, Ni-MDF-0.5, Ni-MDF-1, Ni-MDF-2, and Ni-MDF-4, respectively, as depicted in Fig. S11 and Table 1. The greater ECSA value of Ni-MDF-2 signifies greater availability of active reaction sites for the electrochemical oxidation of methanol.

Another important parameter to quantify the catalytic performance of an electrocatalyst is the roughness factor (RF), which is calculated by dividing the ECSA by the geometrical area of the electrode (roughness factor = ECSA/geometrical area). The higher roughness factor of Ni-MDF-2 clarifies the excellent electrocatalytic behaviour of the catalyst towards methanol oxidation. Furthermore, the specific activity of the electrocatalysts was calculated by dividing the peak current density by the ECSA (specific activity = peak current density/ECSA), as shown in Table 1.

**Table 1** Comparison of ECSA, roughness factor, and specific activity of MDF and Ni-MDF electrocatalysts

| Electrocatalyst | ECSA ($cm^2$) | Specific activity (mA) | Roughness factor |
|---|---|---|---|
| MDF | 0.4725 | 14.18 | 6.75 |
| Ni-MDF-0.5 | 2.336 | 20.54 | 33.37 |
| Ni-MDF-1 | 3.325 | 21.17 | 47.50 |
| Ni-MDF-2 | 7.665 | 14.61 | 109.50 |
| Ni-MDF-4 | 6.606 | 15.14 | 94.37 |

The stability assessment of a catalyst is crucial for its practical application. Chronoamperometry and chronopotentiometry techniques were employed to assess the electrocatalytic stability of the Ni-MDF-2 catalyst. Fig. 8a shows the chronoamperometric plot of the Ni-MDF-2 catalyst in 1.0 M KOH and 0.5 M methanol at a potential of 1.39 V (*vs.* RHE). It is evident from Fig. 8a that the material retained a stable current of 10 mA $cm^{-2}$ over 144 h of extensive study. A potentiometric stability test was also conducted in a solution containing 1.0 M KOH and 0.5 M methanol at 10 mA $cm^{-2}$ (Fig. 8b). The catalyst produced a steady potential of ~1.39 V (*vs.* RHE) for 30 h.

Additionally, the electrocatalytic durability of Ni-MDF-2 was assessed by performing consecutive CV measurements (Fig. S12). Remarkably, the polarisation curve of Ni-MDF-2 showed that the overpotential to achieve 10 mA $cm^{-2}$ current density shifts slightly after 100 consecutive cycles, indicating excellent durability of the catalyst. The excellent stability of the material is attributed to the fact that the active sites of the catalysts remain unobstructed during the electrooxidation of methanol.

The electrochemical parameters for the MOR in alkaline media of Ni-MDF-2 and other catalysts reported previously in the literature are compared and shown in Table S6. It can be concluded that Ni-MDF-2 is an efficient non-noble metal-based catalyst for methanol electrooxidation.

To investigate the interfacial electrochemical behavior during the MOR and the OER, operando electrochemical impedance spectroscopy (EIS) was studied at various potentials (Fig. S13a and b). As displayed in the Bode plots of Ni-MDF-2 (Fig. 9a), no well-defined peak was initially observed in the low-frequency region before 1.40 V *vs.* RHE in the presence of 0.5 M methanol in 1.0 M KOH. The appearance of a peak in the high-frequency region may be attributed to the migration of methanol or hydroxide ($OH^-$) across the Helmholtz plane to the active sites on the electrode surface.[36,67] This process is non-faradaic. When the Bode plot was obtained at 1.40 V *vs.* RHE under the same conditions, a new peak in the low-frequency region was observed, and the peak in the high-frequency region disappeared. The observation indicates the conversion of $Ni^{2+}$ centers responsible for methanol oxidation.[42,67] Similar behavior was observed when operando EIS (Fig. 9b and Fig. S13b) was studied in only 1.0 M KOH after 1.55 V *vs.* RHE, where the $Ni^{3+}$ produced initiated the OER. In the case of the OER process, initially a new peak appeared in the low frequency region. However, the phase angle and diameter decreased at 1.55 V *vs.* RHE, which confirms the occurrence of the OER. However, in the presence of methanol, no new peak appeared in the low frequency region and the MOR process began at 1.40 V *vs.* RHE, demonstrating that the *in situ* generated $Ni^{3+}$ triggered the MOR.[36,42]

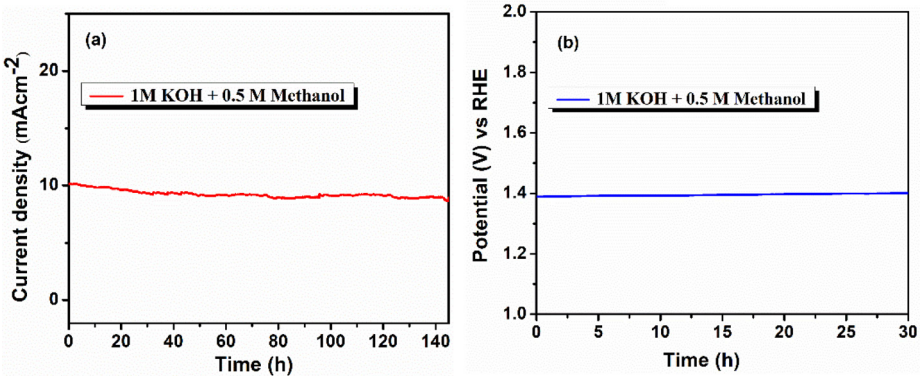


**Fig. 8** (a) Chronoamperometric plot of Ni-MDF-2 in the presence of 0.5 M methanol in 1.0 M KOH at 1.39 V *vs.* RHE and (b) chronopotentiometric plot of Ni-MDF-2 at 10 mA $cm^{-2}$ in the presence of 0.5 M methanol containing 1.0 M KOH.

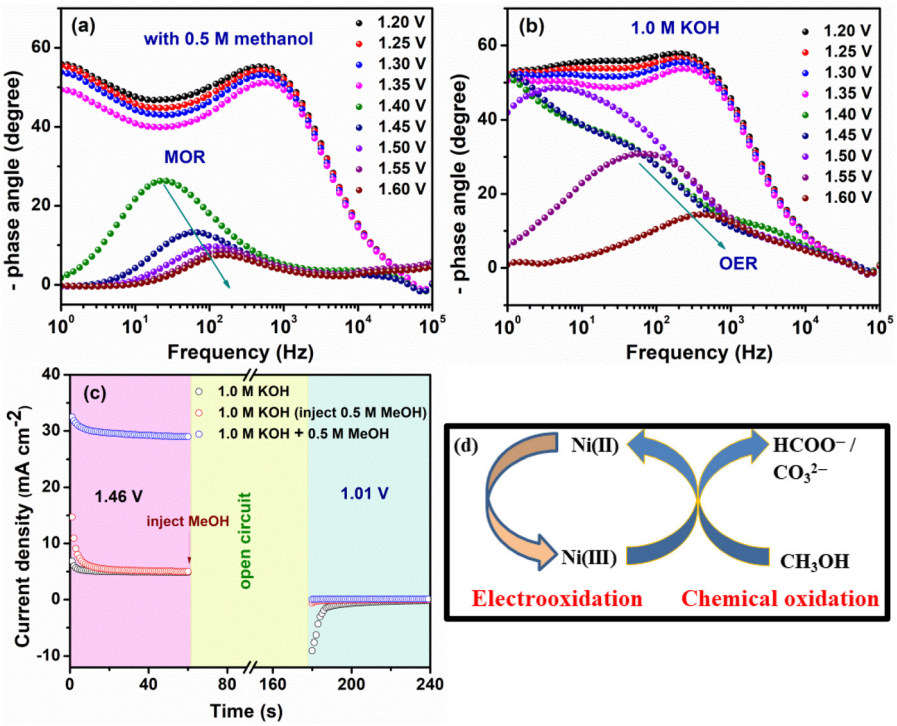


**Fig. 9** Bode plots of operando EIS of Ni-MDF-2 in (a) 1.0 M KOH and 0.5 M methanol and (b) 1.0 M KOH. (c) Multi-potential periodic electrochemical measurements for Ni-MDF-2 at 1.46 V *vs.* RHE (0–60 s), the open circuit state (60–180 s), and 1.01 V *vs.* RHE (180–240 s). (d) Proposed mechanism of the MOR process.

Furthermore, intermittent MOR and OER were performed at different potentials to ascertain the function of high valence $Ni^{3+}$. Initially, a potential of 1.46 V *vs.* RHE was applied for 60 s in 1.0 M KOH (Fig. 9c, black circle) to generate high-valence $Ni^{3+}$ species. The system then remained open-circuit for 120 s, and a potential of 1.01 V *vs.* RHE was applied subsequently. A much higher reduction current was observed under OER conditions, which indicates a non-spontaneous reduction of $Ni^{3+}$ in the absence of methanol. The experiment was repeated with the addition of methanol at 60 s (Fig. 9c, red circle). After the open-circuit state, a negligible reduction current was observed at 1.01 V *vs.* RHE, confirming the spontaneous reduction of $Ni^{3+}$ in methanol. Again, if methanol (0.5 M methanol in 1.0 M KOH) was added at the beginning of the measurement, a much higher current density was observed (Fig. 9c, blue circle) due to the MOR. However, no reduction current was observed after the open-circuit state at 1.01 V *vs.* RHE, indicating instantaneous $Ni^{3+}$ reduction under the MOR conditions. The result is consistent with operando EIS and establishes the mechanism involving electrooxidation of the $Ni^{2+}$ center followed by spontaneous chemical oxidation of methanol by electrochemically generated $Ni^{3+}$ (Fig. 9d).[42,68]

So far, it has been confirmed that surface reconstruction and the formation of high-valence $Ni^{3+}$ occur during both the OER and the MOR. During the surface reconstruction, $Ni(OH)_2$ was initially generated in the presence of $OH^-$, which subsequently converted to high-valence NiOOH. Post-catalytic Raman spectroscopy and XPS were utilized to confirm the generation of NiOOH. Chronoamperometric experiments were conducted in the presence of 1.0 M KOH and 0.5 M MeOH at different potentials for three hours. The sample was collected immediately, and a Raman spectrum was obtained. A pair of featured bands of $Ni^{III}$–O appeared at 465 and 560 $cm^{-1}$ (Fig. S14) at an applied potential of 1.4 V *vs.* RHE and remained dominant as the applied potential increased. The peaks appeared due to the $E_g$ Ni–O bending and $A_{1g}$ Ni–O stretching vibration of $Ni^{III}$–OOH.[36,42]

Furthermore, to confirm the existence of $Ni^{3+}$, XPS analysis was performed with the recovered Ni-MDF-2 catalyst after performing the stability test. XPS analysis revealed the presence of high-valence $Ni^{3+}$ species as depicted in Fig. 10. This result confirms the generation of $Ni^{3+}$ as an intermediate in the MOR process, thereby validating the reaction mechanism.

Post-catalysis PXRD (Fig. S15a) and HRTEM (Fig. S15b) analyses confirmed that the Ni-MDF-2 catalyst preserved its structural and morphological features, demonstrating its robustness under MOR conditions.

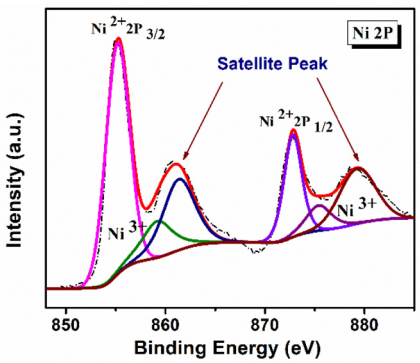


**Fig. 10** Ni 2p XPS spectra of Ni-MDF-2 after a long-term MOR.

Additionally, to identify the potential-determining step (PDS) and rate-determining step (RDS) for the MOR, an H/D kinetic isotope effect (KIE) study was conducted for Ni-MDF-2. The PDS defines the onset potential of the MOR, while the RDS controls the MOR current beyond onset. It is evident that in the presence of $CH_3OH/H_2O$, the catalyst exhibited a low onset potential of 1.38 V *vs.* RHE, followed by a sharp rise in the current density associated with the MOR (Fig. S16). When $CD_3OD/D_2O$ was used instead of $CH_3OH/H_2O$, the catalytic MOR exhibited a shifted onset toward more positive potential and a lower current density (Fig. S16). This positively shifted onset potential suggests that proton-coupled electron transfer (PCET) processes, involving O–H(D) or C–H(D) bond breaking, contribute to the PDS of the methanol oxidation reaction. We further determined the KIE of $J_H/J_D > 2$ within the Tafel region, indicating a normal KIE. This observation indicates that proton-coupled electron transfers are also involved in the RDS of the MOR.[36,42] Thus, the MOR occurs through the subsequent formation of $Ni(OH)_2$ and NiOOH. The reaction proceeds through electrocatalytic Ni(III) generation and chemical oxidation of methanol by high-valence nickel. Accordingly, an indirect mechanism is shown in the SI.

The excellent MOR performance of the Ni-MDF-2 catalyst encouraged us to set up a two-electrode electrolyzer using Ni-MDF-2 as an anode and 5% Pt/C (Fig. S17) as a cathode. The Pt/C||Ni-MDF-2 electrolyzer required 1.46 V (Fig. 11a) to reach a current density of 10 mA $cm^{-2}$ for simultaneous HER||MOR. The stability of the MOR–HER system was assessed using a long-term stability test, and no significant decay in the stability at 1.46 V was observed for 4 h (Fig. 11b).

To gain deeper insight into the product selectivity during extended oxidation, chronoamperometry was performed at a constant potential of 1.39 V *vs* RHE using 2-Ni-MDF electrodes. After 2 h of chronoamperometric testing in 0.5 M methanol containing 1.0 M KOH, the electrolyte obtained was analysed by $^1$H NMR spectroscopy (Fig. 12a). A characteristic peak at 8.3 ppm, consistent with that of a standard formate reference,

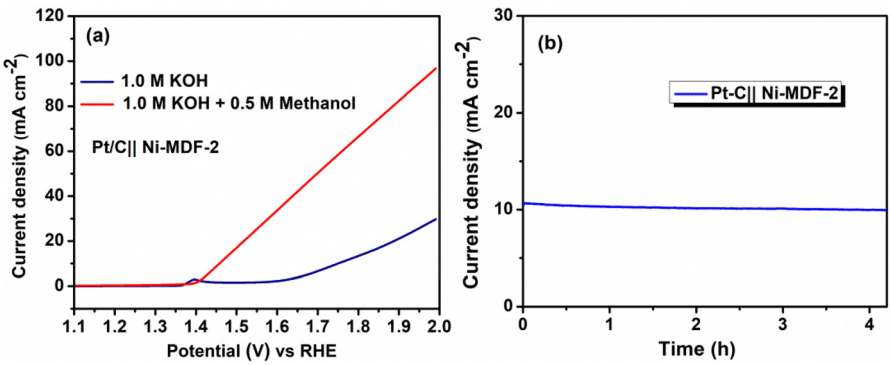


**Fig. 11** (a) LSV curves of a two-electrode electrolyzer involving Pt/C||Ni-MDF-2 and (b) chronoamperometry of the Pt/C||Ni-MDF-2 system in 0.5 M methanol in 1.0 M KOH.

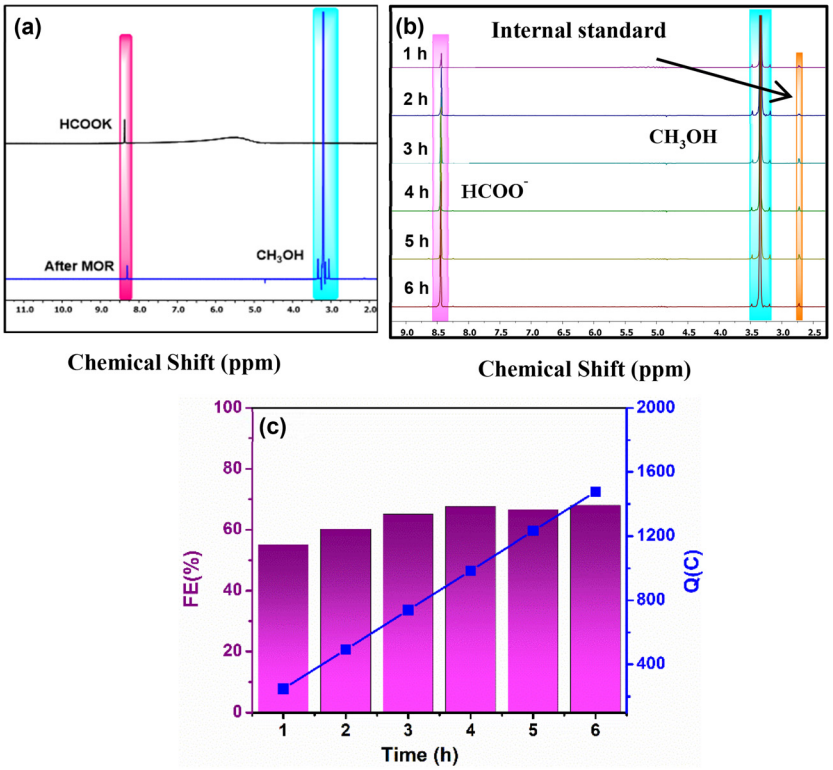


**Fig. 12** (a) $^{1}$H NMR spectrum of the products formed during the methanol oxidation reaction, (b) $^{1}$H NMR spectra recorded after different electrolysis times and (c) the calculated FE of formate production and the corresponding passed charge at different electrolysis durations.

was observed. $^{1}$H NMR analysis revealed formate as a predominant soluble species generated during electrolysis.

Moreover, to quantify formate, a chronoamperometric stability test was performed at 1.56 V *vs.* RHE for different time intervals (1–6 h). Subsequently, quantitative $^{1}$H NMR spectroscopy was used to analyse the collected electrolytes (Fig. 12b). The faradaic efficiency (FE) for formate production was determined from the measured formate concentration and the charge passed in each electrolysis interval. The FE values obtained were 55.16, 60.19, 65.09, 67.6, 66.6, and 68% for 1, 2, 3, 4, 5, and 6 h, respectively (Fig. 12c). The turnover number (TON) and turnover frequency (TOF) of the methanol oxidation reaction were calculated for the 2-Ni-MDF catalyst. The TON and TOF were found to be 191.47 and 31.91 $h^{-1}$.

## Conclusion

In summary, we have demonstrated the successful $Ni^{2+}$ incorporation within a triazine-based porous organic polymer for the electrooxidation of methanol in an alkaline medium. The Ni-MDF catalyst with 4.72 atom% nickel loading (Ni-MDF-2) exhibits the highest electrocatalytic activity with a peak current density of 112 mA $cm^{-2}$ and a low overpotential of 160 mV to achieve 10 mA $cm^{-2}$ current density. The impedance spectroscopy suggests the enhanced charge transfer kinetics of the Ni-MDF-2 catalyst for the methanol oxidation reaction. Additionally, it demonstrates exceptional stability for up to 100 consecutive cycles for the MOR. The Ni-MDF-2 catalyst exhibited exceptional chronoamperometric stability for 144 h. The superior electrocatalytic performance of Ni-MDF catalysts may be ascribed to sufficient exposure to active reaction sites and faster electron transport capability. Furthermore, the involvement of intermediate $Ni^{3+}$ in the MOR was established through operando EIS techniques, which indicates that the electrooxidation of $Ni^{2+}$ to $Ni^{3+}$ occurs, followed by the chemical oxidation of methanol during the MOR. The post-catalytic XPS and Raman spectroscopy further confirm the presence of Ni(III). Additionally, the two-electrode Pt/C||Ni-MDF-2 electrolyzer requires a cell voltage of 1.46 V to achieve 10 mA $cm^{-2}$ current density, which is 280 mV lower than that of the HER–OER system. Moreover, during the MOR, formate is generated as a major product at the anode with 68% faradaic efficiency after 6 h. Thus, the facile synthetic strategy and exceptional electrocatalytic properties of Ni-MDF catalysts hold significant potential for the development of cost-effective, high-efficiency, and non-noble metal-based electrocatalysts for the MOR with the generation of a value-added product.

## Author contributions

I. P. synthesized and characterized the catalysts, performed all the electrochemical measurements and prepared the first draft

of the manuscript. S. D. and S. B. assisted with synthesis, characterization and electrochemical measurements. B. M. performed PXRD, TGA, BET-surface area analysis, and solid- and solution-state NMR analysis. A. B. provided the facility for BET-surface area analysis and TGA, supervised catalyst characterization and checked the draft of the manuscript. P. B. conceptualized and supervised the work, obtained funding and finalized the manuscript.

## Conflicts of interest

The authors declare that there are no conflicts of interest.

## Data availability

All the data are available in the main manuscript or in the supplementary information (SI). The raw data are available on reasonable request from the authors. Supplementary information: details of materials and instrumentation, characterization of MDF and Ni-MDF, and electrochemical experiments. See DOI: https://doi.org/10.1039/d5dt02306h.

## Acknowledgements

I. P., D. G., and S. B. thank the IIEST, Shibpur, for providing a fellowship. P. B. acknowledges the Department of Science & Technology and Biotechnology, Government of West Bengal (DSTBT, GoWB), for financial support (memo no. 2143(Sanc.)/STBT-11012(25)/7/2024-ST SEC dated 10/02/2024). The authors acknowledge the SAIF, IIEST, Shibpur, for providing NMR facility. The authors also sincerely acknowledge the DST FIST for the development of infrastructural facilities of the Department of Chemistry, IIEST, Shibpur (project no. SR/FST/CSI-254/2013 (C), dated: 08/07/2015). The authors express their sincere gratitude to the Central Council for Research in Homoeopathy (CCRH), under the Ministry of AYUSH, Government of India, for establishing the Confocal Raman facility at Dr Bholanath Chakraborty Memorial Fundamental Research Laboratory of Homoeopathy, under the Centre for Healthcare Science & Technology (CHST) at IIEST Shibpur. The authors are also thankful to Dr Sharbadeb Kundu, CHST, for Raman analysis and useful discussion.

## References

1 S. Samanta and A. Pradhan, *Chem. Commun.*, 2025, **61**, 8108–8119.
2 P. Hota, A. Das and D. K. Maiti, *Int. J. Hydrogen Energy*, 2023, **48**, 523–541.
3 H. Tüysüz, *Acc. Chem. Res.*, 2024, **57**, 558–567.
4 Q. Qian, Y. Zhu, N. Ahmad, Y. Feng, H. Zhang, M. Cheng, H. Liu, C. Xiao, G. Zhang and Y. Xie, *Adv. Mater.*, 2024, **36**, 2306108.
5 A. Raveendran, M. Chandran and R. Dhanusuraman, *RSC Adv.*, 2023, **13**, 3843–3876.
6 Y. Lu, L. Tang, P. Wang, M. He, C. Yang and Z. Li, *ACS Catal.*, 2023, **13**, 13804–13815.
7 J. T. Bender, A. S. Petersen, F. C. Østergaard, M. A. Wood, S. M. Heffernan, D. J. Milliron, J. Rossmeisl and J. Resasco, *ACS Energy Lett.*, 2022, **8**, 657–665.
8 T. Liu, C. Xu, Y. Guo, P. Z. Li, S. Yuan and M. Lin, *ACS Appl. Nano Mater.*, 2024, **7**, 9062–9067.
9 J. Huang, M. Li, M. J. Eslamibidgoli, M. Eikerling and A. Groß, *JACS Au*, 2021, **1**, 1752–1765.
10 H. Zhong, Q. Zhang, J. Yu, X. Zhang, C. Wu, Y. Ma, H. An, H. Wang, J. Zhang, X. Wang and J. Xue, *Adv. Energy Mater.*, 2023, **13**, 2301391.
11 A. Mahata, L. Mallick, I. Mehta, N. Kumari, S. Bhattacharya and B. Chakraborty, *J. Mater. Chem. A*, 2025, **13**, 21480–21492.
12 S. Baruah, A. Kumar and N. R. Peela, *J. Electroanal. Chem.*, 2024, **953**, 118015.
13 N. Tanwar, H. Narjinari, H. Sharma, S. Dhole, R. V. Jasra and A. Kumar, *Inorg. Chem.*, 2024, **63**, 3005–3018.
14 M. Li, C. Huang, H. Yang, Y. Wang, X. Song, T. Cheng, J. Jiang, Y. Lu, M. Liu, Q. Yuan, Z. Ye, Z. Hu and H. Huang, *ACS Nano*, 2023, **17**, 13659–13671.
15 X. Xu, L. Su, X. Yu, J. Sun and X. Miao, *Inorg. Chem. Front.*, 2024, **11**, 1381–1393.
16 Z. Zhao, Z. Li, Z. Zhang and X. Meng, *Appl. Catal., B*, 2024, **347**, 123805.
17 S. Xu, D. Jiao, X. Ruan, Z. Jin, Y. Qiu, Z. Feng, L. Zheng, J. Fan, W. Zheng and X. Cui, *Adv. Funct. Mater.*, 2024, **34**, 2401265.
18 M. Zhong, M. Xu, S. Ren, W. Li, C. Wang, M. Gao and X. Lu, *Energy Environ. Sci.*, 2024, **17**, 1984–1996.
19 C. Jo, S. Surendran, M. C. Kim, T. Y. An, Y. Lim, H. Choi, G. Janani, S. C. Jesudass, D. J. Moon, J. Kim, J. Y. Kim, C. H. Choi, M. Kim, J. K. Kim and U. Sim, *Chem. Eng. J.*, 2023, **463**, 142314.
20 S. I. Jacob, A. Chakraborty, A. Chamas, R. Bock, L. Sepunaru and G. Ménard, *ACS Energy Lett.*, 2023, **8**, 3760–3766.
21 H. Chen, J. Song, X. Long, H. You, Y. Weng, D. Liu, Y. Liao, J. Zhang, J. L. Luo and X. Z. Fu, *Appl. Catal., B*, 2025, **361**, 124643.
22 M. Ahmad, M. B. Hussain, J. Chen, Y. Yang, X. Wu, H. Chen, S. Afzal, W. Raza, Z. Zeng, F. Ye, X. Zhao, J. Zhang, R. Feng, X. Z. Fu and J. L. Luo, *ACS Catal.*, 2024, **14**, 9134–9143.
23 S. Dai, M. Li, H. Li, Y. Shi, H. Zhang, D. Wang, K. Xiang and J. Zou, *ChemSusChem*, 2025, **18**, e202402767.
24 L. Chen, X. Liang, D. Wang, Z. Yang, C. T. He, W. Zhao, J. Pei and Y. Xue, *ACS Appl. Nano Mater.*, 2022, **14**, 27814–27822.
25 H. Yang, X. Zhang, H. Zou, Z. Yu, S. Li, J. Sun, S. Chen, J. Jin and J. Ma, *ACS Appl. Nano Mater.*, 2022, **5**, 3275–3288.
26 L. Gong, X. Zhu, T. T. Nga, Q. Liu, Y. Wu, P. Yang, Y. Zhou, Z. Xiao, C. L. Dong, X. Fu, L. Tao and S. Wang, *Angew. Chem., Int. Ed.*, 2024, **63**, e202404713.

27 L. Li, Y. Feng, A. Pei, L. Zhu, W. Wang, Li. Guang, C. Huang, Z. Yang and H. Ye, *ACS Sustainable Chem. Eng.*, 2023, **11**, 8958–8967.
28 Y. Feng, L. Zhu, A. Pei, S. Zhang, K. Liu, F. Wu and W. Li, *Nanoscale*, 2023, **15**, 16904–16913.
29 J. Li, M. Hou and Z. Zhang, *Nanoscale*, 2022, **14**, 8096–8102.
30 X. Ren, Q. Lv, L. Liu, B. Liu, Y. Wang, A. Liu and G. Wu, *Sustainable Energy Fuels*, 2020, **4**, 15–30.
31 N. Narayanan, H. Liu, W. Zhang, B. Ravichandran, Q. Xu, L. Khotseng, Y. Cheng and H. Su, *ACS Appl. Nano Mater.*, 2024, **7**, 3907–3917.
32 L. Han, H. Li, L. Yang, Y. Liu and S. Liu, *ACS Appl. Mater. Interfaces*, 2023, **15**, 9392–9400.
33 P. C. Meenu and S. Roy, *ACS Appl. Energy Mater.*, 2023, **6**, 11212–11225.
34 H. Huang, D. Xiao, Z. Zhu, C. Zhang, L. Yang, H. He, J. You, Q. Jiang, X. Xu and Y. Yamauchi, *Chem. Sci.*, 2023, **14**, 9854–9862.
35 J. Qin, H. Huang, J. Zhang, F. Zhu, L. Luo, C. Zhang, L. Yang, Q. Jiang and H. He, *J. Mater. Chem. A*, 2023, **11**, 2848–2856.
36 K. Deng, P. Liu, X. Liu, H. Li, W. Tian and J. Ji, *Green Chem.*, 2023, **25**, 9837–9846.
37 J. Li, L. Li, J. Wang, A. Cabot and Y. Zhu, *ACS Energy Lett.*, 2024, **9**, 853–879.
38 F. Sheikh, A. Arshad, F. Marriam, Z. Ahmad, A. Haider, M. Iqbal and M.A. Mansoor, *New J. Chem.*, 2023, **47**, 17970–17983.
39 C. Wang, L. Chai, X. Cui, Z. Zhou and S. Liu, *J. Phys. Chem. C*, 2021, **125**, 21443–21452.
40 K. Zhang, Y. Han, J. Qiu, X. Ding, Y. Deng, Y. Wu, G. Zhang and L. Yan, *J. Colloid Interface Sci.*, 2023, **630**, 570–579.
41 Y. Qi, Y. Zhang, L. Yang, Y. Zhao, Y. Zhu, H. Jiang and C. Li, *Nat. Commun.*, 2022, **13**, 4602.
42 B. Zhu, B. Dong, F. Wang, Q. Yang, Y. He, C. Zhang, P. Jin and L. Feng, *Nat. Commun.*, 2023, **14**, 1686.
43 Z. Duan, T. Ren, Q. Mao, H. Yu, K. Deng, Y. Xu, Z. Wang, L. Wang and H. Wang, *J. Mater. Chem. A*, 2022, **10**, 18126–18131.
44 M. Wang, C. Wang, L. Zhu, F. Rong, L. He, Y. Lou and Z. Zhang, *Appl. Catal., A*, 2021, **619**, 118159.
45 S. Liu, Y. Y. Sun, Y. P. Wu, Y. J. Wang, Q. Pi, S. Li, Y. S. Li and D. S. Li, *ACS Appl. Mater. Interfaces*, 2021, **13**, 26472–26481.
46 S. N. Bhaduri, D. Ghosh, R. Chatterjee, S. Das, I. Pramanick, A. Bhaumik and P. Biswas, *Inorg. Chem.*, 2023, **62**, 12832–12842.
47 M. I. Abdullah, A. Hameed, N. Zhang, M. H. Islam, M. Ma and B. G. Pollet, *ACS Appl. Mater. Interfaces*, 2021, **13**, 30603–30613.
48 L. Luo, S. Liu, H. Li and B. Xia, *Energy Fuels*, 2023, **37**, 18030–18037.
49 S. A. Khanam, N. Hoque, S. Lee, Y. B. Park, G. Gogoi and K. K. Bania, *ACS Appl. Energy Mater.*, 2022, **5**, 12651–12662.
50 C. Yao, M. Li, Z. Xue, Z. Yang, K. He, Q. Chen, B. Cheng, R. Wang, S. Cai, X. Qiao, M. Zhang and X. Li, *ACS Appl. Nano Mater.*, 2024, **7**, 19628–19636.
51 D. S. Abraham, M. Chandran, M. Vinoba, R. Yamuna and M. Bhagiyalakshmi, *Langmuir*, 2023, **39**, 4756–4765.
52 O. Lebedeva, D. Kultin, V. Zakharov, I. Kuznetsova, L. Aslanov and L. Kustov, *Sustainable Energy Fuels*, 2025, **9**, 1464–1479.
53 S. Ruidas, B. Mohanty, P. Bhanja, E. S. Erakulan, R. Thapa, P. Das, A. Chowdhury, S. K. Mandal, B. K. Jena and A. Bhaumik, *ChemSusChem*, 2021, **14**, 5057–5064.
54 P. Bhanja, K. Bhunia, S.K. Das, D. Pradhan, R. Kimura, Y. Hijikata, S. Irle and A. Bhaumik, *ChemSusChem*, 2017, **10**, 921–929.
55 O. Ali, A. Jana, A. Das, S. K. Dey and A. Bhunia, *Mater. Adv.*, 2024, **5**, 4720–4727.
56 A. Jana, A. Maity, A. Sarkar, B. Show, P. A. Bhobe and A. Bhunia, *J. Mater. Chem. A*, 2024, **12**, 5244–5253.
57 J. Liu, C. Wang, Y. Song, S. Zhang, Z. Zhang, L. He and M. Du, *J. Colloid Interface Sci.*, 2021, **591**, 253–263.
58 M. Punniyamoorthy, S. Singha Roy, M. Kathiresan and S. Kundu, *ACS Appl. Energy Mater.*, 2024, **7**, 4111–4120.
59 T. Boruah, S. K. Das, G. Kumar, S. Mondal and R. S. Dey, *Chem. Commun.*, 2022, **58**, 5506–5509.
60 R. R. Gagne, C. L. Spiro, T. J. Smith, C. A. Hamann, W. R. Thies and A. D. Shiemke, *J. Am. Chem. Soc.*, 1981, **103**, 4073–4081.
61 S. K. Das, P. Bhanja, S. K. Kundu, S. Mondal and A. Bhaumik, *ACS Appl. Mater. Interfaces*, 2018, **10**, 23813–23824.
62 D. Chakraborty, R. Chatterjee, S. Mondal, S. K. Das, V. Amoli, M. Cho and A. Bhaumik, *ACS Appl. Mater. Interfaces*, 2023, **15**, 48326–48335.
63 M. Stredansky, E. Turco, Z. Feng, R. Costantini, G. Comelli, A. Verdini, L. Floreano and A. Morgante, *Nanoscale Adv.*, 2019, **1**, 1721–1725.
64 K. Artyushkova, B. Kiefer, B. Halevi, A. Knop-Gericke, R. Schlogl and P. Atanassov, *Chem. Commun.*, 2013, **49**, 2539–2541.
65 A. Moysiadou, S. Lee, C. S. Hsu, H. M. Chen and X. Hu, *J. Am. Chem. Soc.*, 2020, **142**, 11901–11914.
66 C. C. McCrory, S. Jung, J. C. Peters and T. F. Jaramillo, *J. Am. Chem. Soc.*, 2013, **135**, 16977–16987.
67 Q. Wen, Y. Lin, Y. Yang, R. Gao, N. Ouyang, D. Ding, Y. Liu and T. Zhai, *ACS Nano*, 2022, **16**, 9572–9582.
68 H. Qin, Y. Ye, J. Li, W. Jia, S. Zheng, X. Cao, G. Lin and L. Jiao, *Adv. Funct. Mater.*, 2023, **33**, 2209698.